LLNL-JRNL-777661

LAWRENCE
LIVERMORE
NATIONAL
LABORATORY

# Efficient IMEX Runge-Kutta Methods for Nonhydrostatic Dynamics

A. Steyer, C. J. Vogl, M. Taylor, O. Guba

June 12, 2019

SIAM Jounal on Scientific Computing

# EFFICIENT IMEX RUNGE-KUTTA METHODS FOR NONHYDROSTATIC DYNAMICS*

ANDREW STEYER†, CHRISTOPHER J. VOGL‡, MARK TAYLOR§, AND OKSANA GUBA¶

**Abstract.** We develop new implicit-explicit Runge-Kutta (IMEX RK) methods for integrating horizontally explicit, vertically implicit (HEVI) partitionings of nonhydrostatic atmosphere models (HEVI models). These new methods, termed IMKG methods, are IMEX RK methods whose explicit part has optimal or near-optimal stability on the imaginary axis and whose implicit part is I-stable. A specialized stability region is presented for characterizing the stability of IMKG and other IMEX methods integrating HEVI models. Subsequently, we formulate two families of IMEX RK methods to enable deriving IMKG methods with a high explicit stage count for integrating HEVI models with large, stable time-steps. We then derive a HEVI partitioning of the HOMME-NH nonhydrostatic model and use this model to compare the accuracy and efficiency of several IMKG methods with other IMEX RK methods from the literature.

**Key words.** implicit-explicit method, IMEX method, semi-implicit, Runge-Kutta method, time-integration, HEVI, nonhydrostatic, global model, atmosphere model

**AMS subject classifications.** 65L04, 65L05, 65L06, 65L07, 65L20, 65M20, 86A10

## 1. Introduction.

The atmosphere is home to various physical processes evolving on a number of time-scales. Consequently, method-of-lines discretizations of partial differential equation (PDE) models of atmospheric flow often result in stiff and multirate initial value problems (IVPs). This occurs in nonhydrostatic modeling where fast vertically propagating acoustic waves can restrict the step-size of explicit time-

*Support for this work was provided by the Department of Energy, Office of Science Scientific Discovery through Advanced Computing (SciDAC) project "A Non-hydrostatic Variable Resolution Atmospheric Model in ACME."

Sandia National Laboratories is a multi-mission laboratory managed and operated by National Technology and Engineering Solutions of Sandia, LLC., a wholly owned subsidiary of Honeywell International, Inc., for the U.S. Department of Energy's National Nuclear Security Administration under contract DE-NA0003525. This paper describes objective technical results and analysis. Any subjective views or opinions that might be expressed in the paper do not necessarily represent the views of the U.S. Department of Energy or the United States Government.

This work was performed under the auspices of the U.S. Department of Energy by Lawrence Livermore National Laboratory under Contract DE-AC52-07NA27344. LLNL-JRNL-777661.



†Computational Science, Sandia National Laboratories, Albuquerque, New Mexico, USA, (asteyer@sandia.gov).

‡Center for Applied Scientific Computing, Lawrence Livermore National Laboratory, Livermore, California, USA (vogl2@llnl.gov).

§Computational Science, Sandia National Laboratories, Albuquerque, New Mexico, USA, (mataylo@sandia.gov).

¶Computational Science, Sandia National Laboratories, Albuquerque, New Mexico, USA, (onguba@sandia.gov).

stepping methods under what is needed for accurate forecasting and climate prediction. Because of this, nonhydrostatic models often employ horizontally explicit, vertically implicit (HEVI) partitioning. In HEVI partitioning (see the references at the end of this section), terms are additively grouped into fast terms corresponding to vertical acoustic wave propagation and relatively slow terms independent of this motion. There are many alternatives to traditional implicit methods for discretizing such partitioned IVPs including implicit-explicit (IMEX), exponential, and multirate methods. These alternatives can circumvent the step-size restrictions of standard explicit methods, often at a much lower computational cost than fully implicit methods. In this paper we develop a family of IMEX Runge-Kutta (RK) methods for integrating nonhydrostatic atmosphere models with a HEVI partitioning (HEVI models). We then develop a HEVI partitioning of the HOMME-NH nonhydrostatic model (see the references below) and compare the performance of IMEX RK methods, both derived herein and from the literature, for its integration.

Our main contribution is to develop a new type of IMEX RK method, referred to as IMKG methods, for the integration of HEVI models. IMKG methods are IMEX RK methods whose explicit part has optimal or near-optimal stability on the imaginary axis and whose implicit part is I-stable [17, Section IV.3, pp. 42-43]. Their name and development is motivated by the work of Kinnmark and Gray (see [23, 24] and also [38] and [19]) who determined stability polynomials for explicit RK methods to have optimal or near-optimal stability on the imaginary axis. Conventional wisdom suggests time truncation errors are dwarfed by spatial truncation and other errors in global atmospheric modeling. We therefore focus on deriving IMKG methods capable of taking large, stable time-steps with the potential trade-off of some accuracy. To do so we derive IMKG methods with a high explicit stage count that also have good coupled IMEX stability. We characterize coupled IMEX stability for HEVI models in Section 2.3 with a specialized stability test equation (Equation 2.5). This test equation, originating in [5, 26, 42], was derived for studying stability properties of IMEX methods integrating HEVI models. To do so, we derive IMKG methods with a high explicit stage count that also have good coupled IMEX stability, which we characterize in Section 2.3 with a specialized stability test equation (Equation 2.5). This test equation, originating in [5, 26, 42], was derived for studying stability properties of IMEX methods integrating HEVI models.

Two families of IMKG methods are considered: the IMKG1 and IMKG2 methods. Both families allow for an arbitrary number of internal stages, and their double Butcher tableaux are structured to enable enable easy parameterization of IMKG methods with a large number of explicit stages in terms of a few free method coefficients (see Example 3.1). The accuracy and explicit stability of IMKG1 and IMKG2 methods is studied in Section 3.2. The IMKG1 methods (Equation 3.1) we consider are second or third order accurate. They are defined so that the number of implicit solves per time-step can be fewer than the number of explicit function evaluations. The IMKG2 methods (Equation 3.2) we consider are second order accurate and the implicit and explicit method have the same stage-time vector. However, IMKG2 methods typically require an implicit solve at every nontrivial internal stage. Double Butcher tableaux for the most efficient IMKG1 and IMKG2 methods we derived are given in the appendix (Section 7, Equations (7.1)-(7.6)).

In Section 4 we develop a HEVI partitioning for the HOMME-NH nonhydrostatic atmosphere model [31, 41]. The governing equations (Equation (4.1)) of HOMME-NH support vertically propagating acoustic waves that require stable numerical treatment. The stiff terms generating these waves are isolated to the equations for vertical momentum and geopotential. This results (Section 4.2) in a HEVI IMEX partitioning where the implicitly treated terms require the solution of relatively simple nonlinear equations that are independent of horizontal derivatives. The nonlinear solvers can then be implemented without horizontal parallel communication.

The performance of several IMKG1 and IMKG2 methods integrating HOMME-NH with the HEVI partitioning we develop is investigated in Section 5 using two tests (Tests 2.0 and 3.1) from the 2012 Dynamical Core Model Intercomparison Project (DC12) [35]. We compare the accuracy and efficiency of several IMKG methods with other methods from the literature (see [10,12,34,41]). Generally speaking, the IMKG1 and IMKG2 methods we derive are capable of stably running with larger step-sizes and have a faster time-to-solution than those to which we compare from the literature (see Sections 5.3.1-5.3.2). However, the IMKG1 and IMKG2 methods can be less accurate than these other methods, even when running with the smaller step-sizes to which those methods are restricted (see Figures 1-2).

Our focus on IMEX methods is motivated by their frequent use in models of geophysical fluid flow [5, 9, 11, 12, 13, 26, 28, 34, 42]. Order conditions for various partitioned and IMEX methods were derived in [15]. We use the formulas given in [21] that, under certain simplifying assumptions, express the order conditions of IMEX RK methods concisely in terms of their double Butcher tableaux. Understanding stability properties of IMEX methods is important for deriving efficient methods and has been extensively studied (see e.g. [2, 8, 16]). We exploit the technique, dating back at least to the early 1970s [37], of increasing the maximum stable step-size by increasing the number of explicit stages. The analysis pioneered in [5, 26, 42] is then used as a heuristic to develop methods capable of taking large stable time-steps when integrating HEVI models.

The HOMME-NH nonhydrostatic model used to evaluate the IMKG methods we derive is based on the spectral element hydrostatic HOMME dynamic core [4, 7, 33]. Semi-implicit and IMEX time-integration strategies have been employed in such nonhydrostatic atmosphere models for many years (see e.g. [28, 30]). These strategies avoid some of the computational costs associated with using a fully implicit time-stepping method [6] or a modified equation set [3]. HEVI partitioning is a popular semi-implicit strategy for nonhydrostatic models [1, 5, 9, 26, 28, 42]. In HEVI partitioning, stiff vertically propagating acoustic waves are treated implicitly with everything else handled explicitly. This allows the use of much larger stable time-steps than standard explicit methods, but with computationally cheaper solves than those required by standard implicit methods.

## 2. Implicit-explicit Runge-Kutta methods.

**2.1. Formulation.** Consider an ordinary differential equation (ODE) that is additively partitioned:

$$\dot{\xi} = f(\xi, t) \equiv n(\xi, t) + s(\xi, t), \quad f, n, s : \mathbb{R}^d \times \mathbb{R} \to \mathbb{R}^d, \tag{2.1}$$

where $d \in \mathbb{N}$ and $\dot{\xi}$ is the derivative of $\xi = \xi(t)$ with respect to $t$. Given $r \in \mathbb{N}$ and real-valued arrays $b, \hat{b}, c, \hat{c} \in \mathbb{R}^r$ and $A, \hat{A} \in \mathbb{R}^{r\times r}$ where $\hat{A}$ is lower triangular and $A$ is strictly lower triangular, we consider $r$-stage IMEX RK methods for approximating IVPs of (2.1) with initial condition $\xi(t_0) = \xi_0$ defined by

$$\begin{cases} \xi_{m+1} = \xi_m + \Delta t \sum_{k=1}^{r} (b_k n_{m,k} + \hat{b}_k s_{m,k}) \\ g_{m,j} = E_{m,j} + \Delta t \hat{A}_{j,j} s_{m,j}, \quad j = 1, \ldots, r, \quad m \in \{0\} \cup \mathbb{N}, \end{cases} \tag{2.2}$$

where $\Delta t > 0$ is the step-size, $n_{m,k} := n(g_{m,k}, t_m + c_k\Delta t)$, $s_{m,k} := s(g_{m,k}, t_m + \hat{c}_k\Delta t)$, $t_{m+1} := t_m + \Delta t$, and

$$E_{m,j} := \begin{cases} \xi_m & j = 1 \\ \xi_m + \Delta t \sum_{k=1}^{j-1}(A_{j,k}n_{m,k} + \hat{A}_{j,k}s_{m,k}) & j = 2, \dots, r. \end{cases}$$

We represent (2.2) with a double Butcher tableau:

$$\begin{array}{c|c} c & A \\ \hline & b^T \end{array} \quad \begin{array}{c|c} \hat{c} & \hat{A} \\ \hline & \hat{b}^T \end{array}. \tag{2.3}$$

The vectors $c$, $\hat{c}$ are called the stage-time vectors and the arrays $A$, $\hat{A}$ are called the Runge-Kutta matrices. The explicit RK method $\begin{array}{c|c} c & A \\ \hline & b^T \end{array}$ is called the explicit method of (2.2) and the implicit RK method $\begin{array}{c|c} \hat{c} & \hat{A} \\ \hline & \hat{b}^T \end{array}$ is called the implicit method of (2.2). We make the following standard simplifying assumption for the remainder of the paper: the $j^{th}$ component of $c$ (resp. $\hat{c}$) is equal to the sum of the $j^{th}$ row of $A$ (resp. of $\hat{A}$). If $\hat{A}$ has $\nu < r$ nonzero diagonal entries, then we say that (2.2) has $\nu$ implicit stages.

**2.2. Stability of explicit RK methods on the imaginary axis.** The stability theory of explicit RK methods for hyperbolic PDEs is a well-established subject [39]. Given real numbers $a < b$ let $i \cdot [a, b] := \{z \in \mathbb{C} : z = i\zeta, \zeta \in [a, b]\}$ where $i := \sqrt{-1}$. For an explicit RK method with stability region $\mathcal{S}$ we define $\sigma_{\max} := \max\{y \geq 0 : i \cdot [-y, y] \in \mathcal{S}\}$ and for IMEX RK methods we use the same symbol $\sigma_{\max}$ to denote the value of $\max\{y \geq 0 : i \cdot y \in \mathcal{S}_e\}$ where $\mathcal{S}_e$ is the stability region of its explicit method. The following theorem bounds the intersection of the stability region of an explicit RK method with the imaginary axis.

THEOREM 2.1. *For an $r$-stage ($r \geq 2$) explicit RK method, $\sigma_{max} \leq r - 1$.*

For a proof refer to [19, Theorem 5.1], [40, Theorem 2], or [38, Chapter 4]. Let $r \geq 2$. The stability polynomials achieving the optimal stability limit ($\sigma_{\max} = r - 1$), referred to as the KGO (Kinnmark and Grey optimal) polynomials, are given in [23, Table 1]. We also employ the third and fourth order accurate KGNO (Kinnmark and Grey near optimal) polynomials [24, Table 1] for which $\sigma_{\max} = \sqrt{(r-1)^2 - 1}$ when KGO polynomials do not attain the desired order of accuracy.

**2.3. H-stability regions and IMKG methods.** We use the following test equation to characterize the stability of IMEX methods integrating atmospheric models with a HEVI splitting (see [5, 26, 42]):

$$\dot{\xi} = -ik_x\mathcal{N}\xi - ik_z\mathcal{S}\xi, \quad \mathcal{N} = \begin{bmatrix} 0 & 0 & 1 \\ 0 & 0 & 0 \\ 1 & 0 & 0 \end{bmatrix}, \quad \mathcal{S} = \begin{bmatrix} 0 & 0 & 0 \\ 0 & 0 & 1 \\ 0 & 1 & 0 \end{bmatrix}, \quad k_x, k_z \geq 0 \tag{2.4}$$

Using Equation (2.4) as a stability test equation for nonlinear PDEs modeling a nonhydrostatic atmosphere is justified via linearization [5, 26, 42]. Equation (2.4) represents the evolution of an acoustic wave in two dimensions in the $(k_x, k_z)$ direction. The range of values for $k_x$, $k_z$ is determined by the normal modes of the linearizations of the explicit and implicit parts of the HEVI partitioning. We let $K_x$ and $K_z$ denote the range of values of $k_x$ and $k_z$ respectively. A typical target application for the HOMME-NH nonhydrostatic model (described in Section 4.1) has a vertical resolution of around 100m and a horizontal resolution around 10km. Thus, we expect $k_x = \mathcal{O}(0.1)$, $k_z = \mathcal{O}(10)$ so that $K_x = [0, \mathcal{O}(0.1)]$, $K_z = [0, \mathcal{O}(10)]$.

We now describe how we use Equation (2.4) to characterize stability of IMEX RK methods for HEVI models. Approximating an IVP of Equation (2.4) with the method (2.2), initial value $\xi(0) = \xi_0$, and step-size $\Delta t > 0$ results in:

$$\xi_{m+1} = R_H(\Delta t k_x, \Delta t k_z)\xi_m, \quad m \in \{0\} \cup \mathbb{N}, \quad k_x \in K_x, \quad k_z \in K_z,$$

where the stability matrix $R_H$ is defined by

$$R_H(x, z) = I_3 - i(b^T \otimes x\mathcal{N} + \hat{b}^T \otimes z\mathcal{S})(I_{3r} + A \otimes ix\mathcal{N} + \hat{A} \otimes iz\mathcal{S})^{-1}(\mathbf{1}_r \otimes I_3), \tag{2.5}$$

where for $w \in \mathbb{N}$, $I_w$ is the $w \times w$ identity matrix and $\mathbf{1}_w := (1, \dots, 1)^T \in \mathbb{R}^w$ and $\otimes$ represents the Kronecker product. The HEVI or H-stability region is defined as

$$\mathcal{S}_H := \{x, z \geq 0 : \text{ each eigenvalue of } R_H(x, z) \text{ is at most 1 in modulus}\}.$$

We also define the set $\mathcal{T}_H$ and $\tau_{\max}$ as follows:

$$\mathcal{T}_H = \{\xi \geq 0 : (x, z) \in \mathcal{S}_H \text{ for all } x \leq \xi, z \geq 0\}, \quad \tau_{\max} := \max(\mathcal{T}_H).$$

Stable time-steps $\Delta t$ are those for which $(\Delta t k_x, \Delta t k_z) \in \mathcal{S}_H$ for all $(k_x, k_z) \in K_x \times K_z$. The set $\mathcal{T}_H$ is the sub-region of $\mathcal{S}_H$ where stability is determined by $K_x$ independent of $K_z$. This is useful for us because in our application we expect that $\max K_z \approx 100 \max K_x$. For two methods we would predict the ratio of their maximum stable step-sizes to approximately be the ratio of their respective values of $\tau_{\max}$.

We regard the H-stability region, $\mathcal{T}_H$, and $\tau_{\max}$ as heuristic tools for deriving IMEX methods capable of taking large, stable time-steps in HEVI models. Because the applications we are targeting are nonlinear and Equation (2.4) is justified via linearization, we cannot expect the H-stability region to give exact estimates for the maximum stable time-step of a method. Furthermore, the stability theory provides no measure of accuracy and some methods we derive can be relatively inaccurate when running close to their empirically determined stability limit (see Table 2 in Section 5.3.2). However, results we obtain in Tables 1-2 validate the use of $\tau_{\max}$ for obtaining a rough estimate the maximum stable step-size.

We close this section with a discussion of desirable stability properties for IMEX methods integrating HEVI models and define the family of IMKG methods. For an $r$-stage IMEX RK method, Theorem 2.1 implies that $\tau_{\max} \leq r - 1$ where equality is possible only if the stability polynomial of its explicit method is a KGO polynomial. Given $\sigma \in (0, r - 1]$, necessary conditions so that $\tau_{\max} = \sigma$ are:

1. The stability region of the explicit method contains $i \cdot [-\sigma, \sigma]$.
2. The implicit method is I-stable.

This motivates the following following definition.

DEFINITION 2.2. *An IMEX RK method is an IMKG method if:*

1. *Its explicit method has a KGO or KGNO stability polynomial.*
2. *Its implicit method is I-stable.*

## 3. Analysis and Formulation of the IMKG1 and IMKG2 methods.

In this section we formulate and analyze two families of IMKG methods: the IMKG1 and IMKG2 methods.

**3.1. Formulation.** As remarked in Section 2, we assume the $j^{th}$ component of $c$ (resp. $\hat{c}$) is the sum of the entries in the $j^{th}$ row of $A$ (resp. $\hat{A}$). IMKG1 methods are IMKG methods with double Butcher tableaux of the following form (where $q \geq 3$ and array entries are zero unless specified):

$$
\begin{array}{c|ccccc}
0 & & & & & \\
c_1 & \alpha_1 & & & & \\
\vdots & \beta_1 & \ddots & & & \\
 & \vdots & & \alpha_{q-2} & & \\
\vdots & \vdots & & & \alpha_{q-1} & \\
c_q & \beta_{q-1} & & & & \alpha_q \\
\hline
 & \beta_{q-1} & & & & \alpha_q
\end{array}
\qquad
\begin{array}{c|ccccc}
0 & & & & & \\
\hat{c}_1 & \hat{\alpha}_1 & \hat{d}_1 & & & \\
\vdots & \hat{\beta}_1 & \ddots & \ddots & & \\
 & \vdots & & \hat{\alpha}_{q-2} & \hat{d}_{q-2} & \\
\vdots & \vdots & & & \hat{\alpha}_{q-1} & \hat{d}_{q-1} \\
\hat{c}_q & \hat{\beta}_{q-1} & & & & \hat{\alpha}_q \\
\hline
 & \hat{\beta}_{q-1} & & & & \hat{\alpha}_q
\end{array}
\tag{3.1}
$$

IMKG2 methods are IMKG methods whose double Butcher tableaux has the following form (where $q \geq 3$ and array entries are zero unless specified):

$$
\begin{array}{c|ccccc}
0 & & & & & \\
c_1 & \alpha_1 & & & & \\
\vdots & & \ddots & & & \\
 & & & \alpha_{q-2} & & \\
\vdots & & & & \alpha_{q-1} & \\
c_q & \beta & & & & \alpha_q \\
\hline
 & \beta & & & & \alpha_q
\end{array}
\qquad
\begin{array}{c|cccccc}
0 & & & & & & \\
\hat{c}_1 & 0 & \alpha_1 & & & & \\
\vdots & & \ddots & \ddots & & & \\
 & & & 0 & \alpha_{q-2} & & \\
\vdots & & & & 0 & \alpha_{q-1} & \\
\hat{c}_q & \hat{\beta} & \hat{\gamma}_1 & \dots & \dots & \hat{\gamma}_{q-2} & \hat{\alpha}_q \\
\hline
 & \hat{\beta} & \hat{\gamma}_1 & \dots & \dots & \hat{\gamma}_{q-1} & \hat{\alpha}_q
\end{array}
\tag{3.2}
$$

where $\hat{\gamma}_j \neq 0$ for at most one $j \in \{1, \dots, q-1\}$. IMKG2 methods with $\hat{\alpha}_q \neq 0$ require an implicit solve after every explicit stage (see the discussion following Equation (3.4) in Section 3.2) while IMKG1 methods do not. Additionally we were able to derive efficient third order accurate IMKG1 methods, but were only able to obtain efficient second order accurate IMKG2 methods. Despite these drawbacks, IMKG2 methods have the desirable property that $c = \hat{c}$ (as long as the method is first order accurate) so that quantities useful in atmospheric modeling that are computed through an equation of state (e.g. temperature or pressure) are easier to approximate at internal stage times. Additionally, the IMKG2 methods we tested were typically more accurate than the second order accurate IMKG1 methods (see Figures 1-2 in Section 5).

There are two main reasons we structure IMKG methods with Equations (3.1)-(3.2) above. Firstly, it enables quick and easy parameterization of second or third order accurate families of methods where $q$ is large ($q > 3$, see Example 3.1 below) in terms of several free method coefficients. Secondly, they are low-storage in the sense that they only require storing two or three solution vectors per stage. This reduces memory read/writes that can be much more expensive than flops on large parallel computers. There may exist low-storage IMKG methods whose double Butcher tableaux are not of the form of Equations (3.1)-(3.2). Such methods are not investigated in this paper but could potentially have fourth or higher order accuracy with comparable stability properties to the methods we derive herein.

We denote the methods we derive in this paper by IMKGj-pEI where:

- $j \in \{1, 2\}$ denotes if the method is an IMKG1 or IMKG2 method.
- $p$ is the order of accuracy of the method.
- $E$ is the number of explicit stages.

- $I$ is the number of nontrivial implicit stages.

**3.2. Stability and accuracy of IMKG1 and IMKG2 methods.** We focus on second and third order accuracy since fourth order accuracy requires satisfaction of an additional 52 order condition equations [21, pp. 43-44]. It is challenging to satisfy this many order conditions with double Butcher tableaux of the form of Equations (3.1)-(3.2) unless $q$ is taken to be very large. Before considering the accuracy of IMKG1 and IMKG2 methods we briefly discuss their explicit stability. The stability polynomial $P_1(z)$ of the explicit method of an IMKG1 method (3.1) is given by:

$$P_1(z) = 1+(\beta_{q-1}+\alpha_q)z+\alpha_q(\beta_{q-2}+\alpha_{q-1})z^2+\ldots+\alpha_q\cdot\ldots\cdot\alpha_2(\beta_1+\alpha_2)z^{q-1}+\alpha_q\cdot\ldots\cdot\alpha_1 z^q. \quad (3.3)$$

If $\beta_k = 0$ for $k = 1, \ldots, q-1$ (which restricts the order of accuracy to at most two), then $\alpha_1, \ldots, \alpha_q$ are uniquely determined by Equation (3.3) and the KGO or KGNO polynomial of degree $q$. The stability polynomial $P_2(z)$ of the explicit method of an IMKG2 method (3.2) is given by:

$$P_2(z) = 1 + (\alpha_q + \beta_{q-1})z + \alpha_q\alpha_{q-1}z^2 + \ldots + \alpha_1 \ldots \alpha_q z^q. \quad (3.4)$$

The coefficients of KGO and KGNO polynomials are all strictly positive [23,24]. This fact combined with Equations (3.3)-(3.4) implies that $\alpha_q \cdot \ldots \cdot \alpha_1 \neq 0$ and therefore $\alpha_j \neq 0$ for $j = 1, \ldots, q$ for all IMKG1 and IMKG2 methods. Consequently, every explicit stage of an IMKG2 method with $\hat{\alpha}_q \neq 0$ is followed by an implicit solve.

We now consider the accuracy of IMKG2 methods. Consider a method of the form (3.2) and let $l \in \{1, \ldots, q-1\}$ be defined so that $\gamma_j \neq 0$ if and only if $j = l$. Then the method is first order accurate order accurate if and only if

$$\alpha_q + \beta = 1 = \hat{\beta} + \hat{\gamma}_l + \hat{\alpha}_q. \quad (3.5)$$

Second order accuracy requires that in addition to Equation (3.5), the method coefficients satisfy [21, pp 43-44]:

$$\begin{aligned} b^T c = b^T \hat{c} = \alpha_q\alpha_{q-1} = \tfrac{1}{2}, \quad \hat{b}^T\hat{c} = \hat{\alpha}_q(\hat{\beta} + \hat{\gamma}_l + \hat{\alpha}_q) + \hat{\gamma}_l\alpha_l = \tfrac{1}{2}, \\ \hat{b}^T c = \hat{\alpha}_q(\beta + \alpha_q) + \hat{\gamma}_l\alpha_l = \tfrac{1}{2}. \end{aligned} \quad (3.6)$$

Equations (3.5)-(3.6) imply than an IMKG2 method (where $\alpha_j \neq 0$ for $j = 1, \ldots, q$, as shown above) is second order accurate if and only if

$$\alpha_q\alpha_{q-1} = \frac{1}{2} = (1/2 - \alpha_q)/\alpha_l, \quad \alpha_q + \beta = 1 = \hat{\beta} + \hat{\gamma}_l + \hat{\alpha}_q. \quad (3.7)$$

By similar calculations using the order conditions stated in [21, pp 43-44], we obtain that an IMKG1 method is second order accurate if and only if

$$\left\{ \begin{array}{c} \alpha_q(\beta_{q-2} + \alpha_{q-1}) = \alpha_q(\hat{\beta}_{q-2} + \hat{\alpha}_{q-1} + \hat{d}_{q-2}) = 1/2 \\ \hat{\alpha}_q(\hat{\beta}_{q-2} + \hat{\alpha}_{q-1} + \hat{d}_{q-2}) = \hat{\alpha}_q(\beta_{q-2} + \alpha_{q-1}) = 1/2 \\ \alpha_q + \beta_{q-1} = 1 = \hat{\alpha}_q + \hat{\beta}_{q-1} \end{array} \right. \quad (3.8)$$

where we note that if $\beta_{q-1} = \hat{\beta}_{q-1} = \beta_{q-2} = \hat{\beta}_{q-2} = 0$, then this is equivalent to $\alpha_q = 1 = \hat{\alpha}_q$, $\alpha_{q-1} = 1/2$, and $\hat{\alpha}_{q-1} + \hat{d}_{q-2} = 1/2$; and third order accurate if and only if $\alpha_q = \frac{3}{4} = \hat{\alpha}_q$, $\beta_{q-1} = \frac{1}{4} = \hat{\beta}_{q-1}$, and

$$\left\{ \begin{array}{c} \hat{\alpha}_{q-1}(\hat{\alpha}_{q-2} + \hat{d}_{q-2} + \hat{\beta}_{q-3}) + 2\hat{d}_{q-1}/3 = 2/9 \\ \hat{\alpha}_{q-1}(\alpha_{q-2} + \beta_{q-3}) + 2\hat{d}_{q-1}/3 = 2/9 \\ \alpha_{q-1}(\alpha_{q-2} + \beta_{q-3}) = 2/9 = \alpha_{q-1}(\hat{\alpha}_{q-2} + \hat{d}_{q-2} + \hat{\beta}_{q-3}) \\ \hat{\alpha}_{q-1} + \hat{d}_{q-1} + \hat{\beta}_{q-2} = 2/3 = \alpha_{q-1} + \beta_{q-2}. \end{array} \right. \quad (3.9)$$

We use the following example to demonstrate parametrizing a third order accurate IMKG1 method in terms of several method coefficients.

EXAMPLE 3.1. *We construct a third order accurate IMKG1 method with* $q = 4$. *Equation* (3.9) *implies that* $\beta_3 = \hat{\beta}_3 = 1/4$, $\alpha_4 = \hat{\alpha}_4 = 3/4$, *and*

$$\begin{cases} \hat{\alpha}_3(\hat{\alpha}_2 + \hat{d}_2 + \hat{\beta}_1) + 2\hat{d}_3/3 = 2/9 = \hat{\alpha}_3(\alpha_2 + \beta_1) + 2\hat{d}_3/3, \\ \alpha_3(\hat{\alpha}_2 + \hat{d}_2 + \hat{\beta}_1) = 2/9 = \alpha_3(\alpha_2 + \beta_1), \\ \hat{\alpha}_3 + \hat{d}_3 + \hat{\beta}_2 = 2/3 = \alpha_3 + \beta_2. \end{cases} \tag{3.10}$$

*The third order KGNO (third order accuracy is impossible with the use of a KGO polynomial with* $q = 4$*) polynomial with* $q = 4$ *is given by:*

$$P(z) = 1 + z + z^2/2 + z^3/6 + z^4/24. \tag{3.11}$$

*If the method* (3.1) *is third order accurate, then Equation* (3.3) *implies its stability polynomial is* $P_1(z) = 1 + z + z^2/2 + z^3/6 + \alpha_4\alpha_3\alpha_2\alpha_1 z^4$. *It follows that* $\alpha_4\alpha_3\alpha_2\alpha_1 = 1/24$. *If* $\beta_1$ *and* $\alpha_2$ *are specified with* $\alpha_2 \neq -\beta_1$, *then Equation* (3.10) *and* $\alpha_4 = \frac{3}{4}$ *imply that* $\alpha_3$, $\beta_2$, *and* $\alpha_1$ *are given by*

$$\alpha_3 = \frac{2}{9(\alpha_2 + \beta_1)}, \quad \beta_2 = 2/3 - \alpha_3, \quad \alpha_1 = \frac{1}{18(\alpha_2\alpha_3)}, \quad \hat{\alpha}_3 = \frac{2/9 - 2\hat{d}_3/3}{\alpha_2 + \beta_1}. \tag{3.12}$$

*If* $\hat{d}_2$, $\hat{d}_3$, *and* $\hat{\beta}_1$ *are also specified, then Equation* (3.10) *implies that*

$$\hat{\alpha}_2 = 2/(9\alpha_3) - \hat{d}_2 - \hat{\beta}_1, \quad \hat{\beta}_2 = 2/3 - \hat{\alpha}_3 - \hat{d}_3. \tag{3.13}$$

*The remaining method coefficients,* $\hat{d}_1$ *and* $\hat{\alpha}_1$, *can then be chosen independently of the others. The choice of* $\beta_1 = \hat{\beta}_1 = \hat{d}_1 = \hat{\alpha}_1 = 0$, $\alpha_2 = 2/3$; $\hat{d}_2 = \hat{d}_3 = (3 + \sqrt{3})/6$ *results in the IMKG1-342 method (Equation* (7.3) *in the Appendix). These values were chosen as follows. We let* $\hat{d}_1 = 0$ *so the method only requires two rather than three implicit solves per time-step. We then set* $\beta_1 = \hat{\beta}_1 = \hat{\alpha}_1 = 0$ *to reduce the size of the parameter space. We then set* $d = \hat{d}_2 = \hat{d}_3$ *and searched for values of* $\alpha_2$ *and* $d$ *for which the implicit method was I-stable and the value of* $\tau_{\max}$ *was large (*$\approx 2.32$*) and define the remaining coefficients via Equations* (3.12)-(3.13).

## 4. The HOMME-NH nonhydrostatic model and its HEVI partitioning.

### 4.1. Formulation of HOMME-NH.

A comprehensive derivation of HOMME-NH is given in [31]. It is a variant of the Laprise formulation [25] and uses the shallow atmosphere and traditional approximations (see [36]). The governing equations of HOMME-NH are given by:

(4.1)

$$\begin{cases} \mathbf{u}_t + (\nabla_\eta \times \mathbf{u} + 2\Omega) \times \mathbf{u} + \frac{1}{2}\nabla_\eta(\mathbf{u}\cdot\mathbf{u}) + \dot{\eta}\frac{\partial \mathbf{u}}{\partial \eta} + \frac{1}{\rho}\nabla_\eta p + \mu\nabla_\eta\phi = 0, \quad \dot{\eta} := d\eta/dt \\ w_t + \mathbf{u}\cdot\nabla_\eta w + \dot{\eta}\frac{\partial w}{\partial \eta} + \mathfrak{g}(1-\mu) = 0, \quad \mu := \frac{\partial p}{\partial \eta}/\frac{\partial \pi}{\partial \eta} \\ \phi_t + \mathbf{u}\cdot\nabla_\eta\phi + \dot{\eta}\frac{\partial \phi}{\partial \eta} - \mathfrak{g}w = 0 \\ \Theta_t + \nabla_\eta\cdot(\Theta\mathbf{u}) + \frac{\partial}{\partial \eta}(\Theta\dot{\eta}) = 0, \quad \Theta = \frac{\partial \pi}{\partial \eta}\theta \\ \frac{\partial}{\partial t}(\frac{\partial \pi}{\partial \eta}) + \nabla_\eta\cdot(\frac{\partial \pi}{\partial \eta}\mathbf{u}) + \frac{\partial}{\partial \eta}\left(\frac{\partial \pi}{\partial \eta}\dot{\eta}\right) = 0. \end{cases}$$

The horizontal spatial variables $x, y$ lie on a spherical domain and $\eta$ is the mass-based hybrid terrain-following vertical coordinate introduced in [20]. The vector $\mathbf{v} = (u, v, w)^T$ is the fluid velocity with $\mathbf{u} := (u, v)^T$, $\theta$ is the potential temperature, $\mathfrak{g}$ is the gravitational constant, $\phi = \mathfrak{g}z$ is the geopotential, $\rho$ is the fluid density, $p$ is the pressure, $2\Omega \times \mathbf{u}$ is the Coriolis term with rotation rate $\Omega$, and the symbol $\nabla_\eta$ represents the two-dimensional gradient with respect to $(x, y)^T$ in $\eta$-coordinates. The variable $\pi$ represents the hydrostatic pressure defined so that $\frac{\partial \pi}{\partial z} = -\rho\mathfrak{g}$ with the boundary condition $\pi = \pi_{\text{top}}$ imposed at $\eta = \eta_{\text{top}}$ for some constant $\pi_{\text{top}}$.

We now derive a HEVI partitioning of Equation (4.1). Use of the mass-based vertical coordinate $\eta$ means that oscillations in density will cause oscillations in $\phi$ [25, Appendix A]. In particular, density oscillations from vertical acoustic waves manifest in the physical position of the model $\eta$-layers and are decoupled from vertical motions relative to this moving coordinate system. Therefore, the vertical advection terms (e.g. $\dot{\eta}\frac{\partial w}{\partial \eta}$) are not associated with the fast motions of the vertical acoustic waves. This isolates the vertical acoustic waves to the two non-transport terms in the equations for $w$ and $\phi$ in Equation (4.1). Thus, we choose our HEVI partitioning such that $\mathfrak{g}(1-\mu)$ and $\mathfrak{g}w$ are the only implicitly treated terms. Expressing Equation (4.1) as a general evolution equation

$$\xi_t = f(\xi), \quad \xi = (u, v, w, \phi, \Theta, \partial\pi/\partial\eta)^T, \tag{4.2}$$

we define the HEVI partitioning $f(\xi) = n(\xi) + s(\xi)$ of Equation (4.1) by

$$s(\xi) := (0, 0, -\mathfrak{g}(1-\mu), \mathfrak{g}w, 0, 0)^T, \quad n(\xi) := f(\xi) - s(\xi). \tag{4.3}$$

Essentially, this partitioning additively groups terms into the nonstiff hydrostatic terms $n(\xi)$ and the stiff nonhydrostatic terms $s(\xi)$.

**4.2. IMEX RK integration of HOMME-NH.** We now analyze the stage equations resulting from integrating Equation (4.1) with the HEVI partitioning from Equation (4.3) by an IMEX RK method with step-size $\Delta t > 0$ and initial condition $\xi(0) = \xi_0$. For $j = 1, \ldots, r$ and $m \in \{0\} \cup \mathbb{N}$, we express the internal stages as $g_{m,j} = (g^u_{m,j}, g^v_{m,j}, g^w_{m,j}, g^\phi_{m,j}, g^\Theta_{m,j}, g^{\partial\pi}_{m,j})^T$ where $\partial\pi := \partial\pi/\partial\eta$. Using the notation of Equation (2.2) we write

$$g_{m,j} = E_{m,j} + \Delta t \hat{A}_{j,j} s(g_{m,j}), \quad j = 1, \ldots, r.$$

From the definition of $n$ and $s$, the internal stages for $u$, $v$, $\Theta$, and $\partial\pi/\partial\eta$ are explicit:

$$g^u_{m,j} = E^u_{m,j}, \quad g^v_{m,j} = E^v_{m,j}, \quad g^\Theta_{m,j} = E^\Theta_{m,j}, \quad g^{\partial\pi}_{m,j} = E^{\partial\pi}_{m,j}.$$

On the other hand, determining $g^w_{m,j}$ and $g^\phi_{m,j}$ requires solving the following system:

$$\begin{cases} g^w_{m,j} = E^w_{m,j} + \Delta t \mathfrak{g} \hat{A}_{j,j}(1-\mu_{m,j}) \\ g^\phi_{m,j} = E^\phi_{m,j} + \Delta t \mathfrak{g} \hat{A}_{j,j} g^w_{m,j} \end{cases}, \quad m \in \{0\} \cup \mathbb{N}, \quad j = 1, \ldots, r, \tag{4.4}$$

where $\mu_{m,j} := \mu(g^w_{m,j}, g^\phi_{m,j})$ (recall from Equation (4.1) that $\mu := \frac{\partial p}{\partial \eta} / \frac{\partial \pi}{\partial \eta}$). The second equation in (4.4) is rearranged to

$$g^w_{m,j} = (g^\phi_{m,j} - E^\phi_{m,j})/(\mathfrak{g}\Delta t \hat{A}_{j,j}). \tag{4.5}$$

It follows that $g^w_{m,j}$ is an explicit function of $g^\phi_{m,j}$ and $\mu_{m,j} = \mu(g^\phi_{m,j})$. Substituting Equation (4.5) into the first equation of (4.4) implies that $g^\phi_{m,j}$ is given by

$$g^\phi_{m,j} - E^\phi_m = g\Delta t \hat{A}_{j,j} E^w_m - (\mathfrak{g}\Delta t \hat{A}_{j,j})^2(1-\mu_{m,j}), \quad m \in \mathbb{N}\cup\{0\}, \quad j = 1,\dots,r.$$

Hence we can find $g^\phi_{m,j}$ by solving $G_{m,j}(g^\phi_{m,j}) = 0$ where

$$G_{m,j}(g^\phi_{m,j}) = g^\phi_{m,j} - E^\phi_{m,j} - \mathfrak{g}\Delta t \hat{A}_{j,j} E^w_m + (\mathfrak{g}\Delta t \hat{A}_{j,j})^2(1-\mu_{m,j}). \tag{4.6}$$

We solve Equation (4.6) with Newton's method (described in Section 5.1).

## 5. Implementation and experiments.

**5.1. Spatial discretization and implementation details.** HOMME-NH is implemented in the High Order Method Modeling Environment (HOMME) [4, 7]. Horizontal derivatives (those involving $\nabla_\eta$) are discretized with fourth order spectral elements [33] on the cubed sphere grid [32, Sec. 4]. Vertical derivatives (those involving $\partial/\partial\eta$) are discretized with the second order SB81 Simmons and Burridge [29] method with a Lorenz vertical staggering [27]. We refer readers to [31] for a detailed description of the spatial discretization.

IMEX RK methods are implemented with an interface to the ARKode package [9, 10] of the SUNDIALS library [18]. This interface is a continuation of the one developed for the nonhydrostatic Tempest dynamical core [14]. We compare our best performing IMKG1 and IMKG2 methods (IMKG1-242 (7.1), IMKG1-252 (7.2), IMKG1-342 (7.3), IMKG2-244 (7.4), IMKG2-255 (7.5), IMKG2-266 (7.6)) with several IMEX RK methods from the literature (henceforth called the non-IMKG methods). The non-IMKG methods we consider are the third order accurate ARS343 [2, Sec. 2.7] and ARK324 [22, pp. 47-48] methods and the second order accurate ARK2 [12, Eq. 3.9] and Strang carryover (sometimes abbreviated Str. Car.) [34, Eq. 29-34] methods. In addition to these the third order accurate KGU35 explicit RK method [14, Eq. 56] is used to produce reference solutions for error calculations.

We now describe how the solver for computing the implicit stages $g_{m,j}$ (see the notation in Section 4.2) via Newton's method is implemented. From the initial guess $g^{(0)}_{m,j} = E_{m,j}$, the ARKode package generates iterates $g^{(k+1)}_{m,j}$ of the form $g^{(k+1)}_{m,j} = g^{(k)}_{m,j} + \delta^{(k+1)}_{m,j}$, where $\delta^{(k+1)}_{m,j}$ is the solution of

$$\left[I - \Delta t \hat{A}_{j,j} \partial_\xi s(g^{(k)}_{m,j})\right]\delta^{(k+1)}_{m,j} = E_{m,j}, \quad \partial_\xi s := \partial s/\partial \xi.$$

Recall from Section 4.2 that the only non-zero elements of $\partial_\xi s(g^{(k)}_{m,j})$ are those such that both the row and column pertain to $g^w_{m,j}$ or $g^\phi_{m,j}$. To take advantage of this structure, the ARKode package calls a custom HOMME-NH routine to solve for $\delta^{(k+1)}_{m,j}$ from $E_{m,j}$, $\Delta t$, $\hat{A}_{j,j}$, and $g^{(k)}_{m,j}$. In this custom routine, components of $\delta^{(k+1)}_{m,j}$ not pertaining to $g^w_{m,j}$ or $g^\phi_{m,j}$ are set to the values of the corresponding components of $E_{m,j}$. Components of $\delta^{(k+1)}_{m,j}$ pertaining to $g^\phi_{m,j}$, denoted $\delta^{\phi,(k+1)}_{m,j}$, are computed by decomposing the linear system $J_{m,j}(g^{(k)}_{m,j})\delta^{\phi,(k+1)}_{m,j} = E^\phi_{m,j}$ into the independent tridiagonal blocks for each grid column. The LAPACK routines DGTTRF and DGTTRS are called to solve for $\delta^{\phi,(k+1)}_{m,j}$, which is then used to compute $\delta^{(k+1)}_{m,j}$ via Equation (4.5): $\delta^{(k+1)w}_{m,j} = (\delta^{(k+1)\phi}_{m,j} - E^\phi_{m,j})/(\mathfrak{g}\Delta t \hat{A}_{j,j})$.

The ARKode package generates iterates $\delta_{m,j}^{(k+1)}$ until $R_{m,j}^{(k+1)}\|\delta_{m,j}^{(k+1)}\| < \epsilon$, where

$$R_{m,j}^{(k+1)} = \max\left(0.3R_{m,j}^{(k)}, \frac{\|\delta_{m,j}^{(k+1)}\|}{\|\delta_{m,j}^{(k)}\|}\right), \; \|\delta_{m,j}^{(\cdot)}\| = \left[\frac{1}{N}\sum_{l=1}^{N}\left(\frac{[\delta_{m,j}^{(\cdot)}]_l}{\epsilon_r|[x_{m,j}]_l| + [\epsilon_a]_l}\right)^2\right]^{\frac{1}{2}},$$

$R_{m,i}^{(0)} = 1$, $N$ is the total number of components in $q_m$, and $[\cdot]_l$ indicates selecting the $l^{\text{th}}$ element. Note that $\epsilon$, $\epsilon_r$, and $\epsilon_a$ are all tunable tolerances. The value of $\epsilon$ chosen here is the default ARKode value $\epsilon = 0.1$. We chose $\epsilon_r = 10^{-6}$ by varying the value until the change in solution was negligible. For the absolute tolerances, we chose $\epsilon_a^u = \epsilon_a^v = \epsilon_a^w = 10\epsilon_r$, $\epsilon_a^\phi = 10^5\epsilon_r$, $\epsilon_a^\Theta = 10^6\epsilon_r$, and $\epsilon_a^{\partial\pi/\partial\eta} = \epsilon_r$. Those coefficients correspond to the general expected magnitude of each of the quantities.

Experiments were run on a local computing cluster with a number of dual socket compute nodes. Each socket consists of 18, 2.1 GHz, Intel Broadwell E5-2695 v4 computing cores or 36 cores per node. MPI communication in HOMME-NH happens between horizontal elements but not within vertical columns. Therefore the implicit solves require no parallel communication and tend to become cheaper relative to explicit function evaluations as the number of horizontal elements per computing core (elem/core) decreases. We choose the number of compute nodes for our experiments to be 2 elem/core. This is close to the ratios we expect to use in production simulations so that our experiments are relevant for our applications. Note that efficiency can vary and depends on implementation choices, compiler options, and machine configuration.

**5.2. DC12 tests and predicted maximum step-size.** We run two test cases from D12 [35]: Test 2.0 (D12.2.0, atmosphere at rest with orography) [35, Section 2.0] and Test 3.1 (D12.3.1, nonhydrostatic gravity wave) [35, Section 3]. Both tests can use "small planets" (planets with shrunken radii) to enable testing various horizontal-to-vertical aspect ratios without using computationally expensive high spatial resolution. For both test cases and each IMEX method we associate a value of *maxdt* (the maximum stable step-size an IMEX method was able to take) and *relerr* (the $L^2$ relative error of some quantity when an IMEX method is run with step-size *maxdt* for a given length of time). We empirically determine *maxdt* as the largest step-size with which each method is able to complete a simulation without going unstable. Results for DC12.3.1 are presented before those for DC12.2.0 since the latter proved to be a more challenging problem than the former.

**5.3. Test Results.**

**5.3.1. D12.3.1 Results.** In this test case, the potential temperature field ($\theta$ in Equation (4.1)) of a hydrostatically balanced initial state is perturbed to generate nonhydrostatic gravity waves [35, Section 3]. D12.3.1 uses small planet $\times 125$ and a cubed sphere that is divided into 4374 horizontal elements. With our fourth order spectral element discretization and small planet $\times 125$, this corresponds to a horizontal resolution of about 1km. The atmospheric depth is set to 10km using 20 vertical layers (see [35, Appendix F.3] for the arrangement of the vertical levels) corresponding to a vertical resolution of approximately 0.5km. This corresponds roughly to a 2 : 1 horizontal-to-vertical aspect ratio.

We measure the accuracy of the IMEX methods by comparing the integrated value of $\Theta$ (potential temperature pseudo-density) with that of a reference solution after a 172.8s integration. We highlight the accuracy of $\Theta = \theta\frac{\partial\pi}{\partial\eta}$ since the waves in D12.3.1 result from an initial perturbation in $\theta$. The reference solution is computed by integrating DC12.3.1 forward in time 172.8s using the KGU35 method with step-size $\Delta t = 8 \cdot 10^{-5}$ s and has a relative accuracy of about $10^{-12}$ (see Figure 1, right). We integrate the IMEX RK methods for 172.8s using various step-sizes in the interval $[0.24s, 3.93s]$ (no method completed a 172.8$s$ run with step-size exceeding 3.94s). The error of a method is computed by forming the $L^2$-norm difference of the approximate $\Theta$ with that of the reference solution at the end of the 172.8s run.

Results are displayed in Table 1 and Figure 1. In Table 1 we list $maxdt$, $relerr$, and $\tau_{\max}$ for the IMKG1, IMKG2, and non-IMKG methods. Each method has small relative error ($< 10^{-7}$) when running with step-size $maxdt$. The theoretical prediction from Section 2.3 is that ratio of the maximum stable step-size of two methods should be approximately the ratio of their respective values of $\tau_{\max}$. The ratio of the values of $maxdt$ match this theoretical ratio to about 5% of what would be predicted for the IMKG1 and IMKG2 methods as well as Strang Carryover. However, for the ARK324, ARS343, and ARK2 the theory is somewhat pessimistic and these methods have maximum stable step-sizes about $20 - 40\%$ better than would be predicted.

In Figure 1, we plot the accuracy (relative $L^2$ error of $\Theta$ vs step-size ($\Delta t$), Figure 1, right) and efficiency (relative $L^2$ error of $\Theta$ vs run-time, Figure 1, left) for the IMKG1, IMKG2, and non-IMKG methods. All methods achieve their theoretical order of convergence at the tested step-sizes until reaching the accuracy of the reference solution, with the Strang Carryover method doing somewhat better than its predicted second order accuracy. The IMKG1 and IMKG2 methods are typically less accurate than the non-IMKG methods, with the exceptions of the Strang Carryover method which (which lies between the IMKG2 methods and the second order IMKG1 methods) and the IMKG1-342 method which is more accurate than the second order IMKG and non-IMKG methods and less accurate than the third order non-IMKG methods. The efficiency plot gives a better indication of the relative advantages of the IMKG and non-IMKG methods. The IMKG methods are typically faster, but less accurate than the non-IMKG methods and are positioned further up and left in efficiency plots. However, we do call attention to the IMKG1-342 method which is among the fastest methods, but still quite accurate.

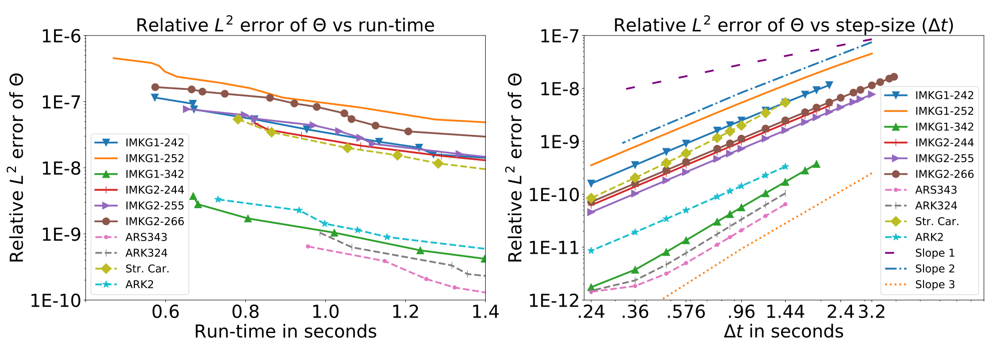


Fig. 1: Results for a 172.8s integration of DC12.3.1. (Left) Relative error of $\Theta$ in the $L^2$-norm vs run-time; (Right) Relative error of $\Theta$ in the $L^2$-norm vs step-size. Slope 1, Slope 2, and Slope 3 in the plot on the right denote lines with slope 1, 2, and 3 respectively and are included for evaluating the order of accuracy of the methods. Accuracy of the reference solution is approximately $10^{-12}$.

Table 1: Values of *maxdt* and *relerr* (defined as in Section 5.2) and $\tau_{\max}$ for various IMKG1, IMKG2, and non-IMKG methods integrating DC12.3.1.

| IMKG | 2-266 | 2-255 | 1-252 | 2-244 | 1-242 | 1-342 |
|---|---|---|---|---|---|---|
| $\tau_{\max}$ | 4.90 | 4.00 | 4.00 | 2.83 | 2.83 | 2.32 |
| maxdt | 3.93 | 3.20 | 3.20 | 2.16 | 2.16 | 1.92 |
| relerr | 1.66E-7 | 7.72E-8 | 4.54E-7 | 4.71E-8 | 1.15E-7 | 3.74E-9 |

| Method | Strang carryover | ARK324 | ARS343 | ARK2 |
|---|---|---|---|---|
| $\tau_{\max}$ | 1.73 | 1.50 | 1.42 | 1.25 |
| maxdt | 1.44 | 1.44 | 1.44 | 1.44 |
| relerr | 5.43E-8 | 1.04E-9 | 6.47E-10 | 5.42E-8 |

**5.3.2. D12.2.0 Results.** This test measures the response to a single circular steep mountain ridge from an initial condition of an atmosphere initially at rest [35, Section 2.0]. D12.2.0 uses small planet $\times 1$ and a cubed sphere divided into 5400 horizontal elements. With the fourth order spectral element horizontal discretization on small planet $\times 1$ this corresponds to a horizontal resolution of about 110km. The atmospheric depth is set to 12km using 30 vertical layers corresponding to a vertical resolution of about 0.4km (see [35, Appendix F.3] for the arrangement of the vertical levels). This corresponds to a horizontal-to-vertical aspect ratio of about 275 : 1.

The accuracy of the IMEX methods is measured by comparing the integrated value of $\partial\pi/\partial\eta$ with that of a reference solution after a 21600s integration. The quantity $\partial\pi/\partial\eta$ represents the vertical hydrostatic pressure gradient in $\eta$-coordinates and its error is highlighted because DC12.2.0 is used for measuring the accuracy of pressure gradient calculations [35, Section 2.0]. The reference solution is formed by integrating DC12.2.0 for 21600s with the KGU35 method using a step-size of $10^{-2}$ seconds and has an accuracy of around $10^{-9}$ (see Figure 2, right). We integrate various IMEX methods on the same time interval using step-sizes in the interval $[7.5s, 583.8s]$ (no method we tested were able to complete a 21600s run with a step-size larger than 583.9s). The error for each method is approximated by forming the $L^2$-norm difference of $\partial\pi/\partial\eta$ with that of the reference solution at the end of the simulation.

Results are displayed in Table 2 and Figure 2. In Table 2, we list *maxdt*, *relerr*, and $\tau_{\max}$ for the IMKG1, IMKG2, and non-IMKG methods. The IMKG2 and non-IMKG methods as well as IMKG1-342 have small relative error ($<$ 1.05E-6) when running with step-size *maxdt*. However, the IMKG1-242 and IMKG1-252 methods are both relatively inaccurate when running with *maxdt* and have values of *relerr* of almost $10^{-3}$. Figure 2 shows that for step-sizes about $10-20\%$ smaller than *maxdt* the relative $L^2$ errors in $\partial\pi/\partial\eta$ of IMKG1-242 and IMKG1-252 reduce to under $10^{-6}$. For the IMKG2 methods the ratios of *maxdt* scale with $\tau_{\max}$ as theoretically predicted in Section 2.3 within of range of about 10% of what is theoretically predicted. Relative to the IMKG2 methods, the value of $\tau_{max}$ overestimates *maxdt* by about 20% for IMKG1-242 and IMKG1-342, 40% for IMKG-252, and by about 30% for the Strang carryover and ARK2 methods and underestimates the value of *maxdt* for ARK324 by about 25% and ARS343 by 42%. The overestimate of *maxdt* for the IMKG1-242 and IMKG1-252 methods can be explained by their relative inaccuracy when running with larger step-sizes. However, the over- and underestimates of *maxdt* for IMKG1-342 and the non-IMKG methods is harder to explain other than concluding that for this test problem the theoretical predictions from Section 2.3 are less exact.

Consider the plot of the accuracy (relative $L^2$ error of $\partial\pi/\partial\eta$ vs step-size, Figure 2, right) for the IMKG1, IMKG2, and non-IMKG methods. The IMKG1 and non-IMKG methods achieve their theoretical order of convergence where with Strang Carryover having slightly higher than its predicted second order accuracy. The second order IMKG1 methods (IMKG1-242 and IMKG1-252) both become inaccurate when running at larger step-sizes ($\Delta t \geq 180$s), although they achieve their theoretical order of accuracy for smaller step-sizes ($\Delta t \leq 90$s). The IMKG2 methods all initially achieve second order accuracy for large ($\Delta t \geq 120$s) step-sizes. Their convergence stagnates at moderate step-sizes before partially recovering between first and second order accuracy for small step-sizes ($\Delta t \leq 45$s). Despite this drawback, the IMKG2 methods still prove to be among the most efficient choices for integrating DC12.2.0.

Consider the plot of efficiency (relative $L^2$ error of $\partial\pi/\partial\eta$ vs run-time, Figure 2, left) of the IMKG1, IMKG, and non-IMKG methods. ARK2 is slow but relatively accurate while the Strang carryover method is slow, but relatively inaccurate. ARS343 and ARK324 are the most accurate methods but are unable to run with the speed of the IMKG1 or IMKG2 methods due to limits on their respective values of $maxdt$. The IMKG1-252 method has the fastest run-times, although this speed comes at the price of having a large relative error (above $10^{-5}$). IMKG1-342 and IMKG2-266 are slightly slower but much more accurate (relative error under 1.04E-6) alternatives to IMKG1-252 that can still run much faster than the non-IMKG methods.

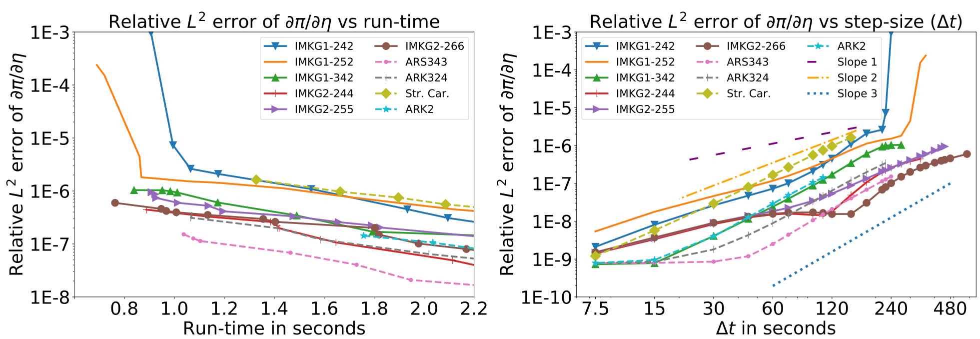


Fig. 2: Results for a 21600s integration of DC12.2.0. Relative error of $\partial\pi/\partial\eta$ in the $L^2$-norm vs run-time (left); $\partial\pi/\partial\eta$ in the $L^2$-norm vs the step-size (right). Slope 1, Slope 2, and Slope 3 in the plot on the right denote lines with slope 1, 2, and 3 respectively and are included for evaluating the order of accuracy of the methods. Accuracy of the reference solution is approximately $10^{-9}$.

Table 2: Values of $maxdt$ and $relerr$ (defined as in Section 5.2) and $\tau_{\max}$ for various IMKG1, IMKG2, and non-IMKG methods integrating DC12.2.0.

| IMKG | 2-266 | 2-255 | 1-252 | 2-244 | 1-242 | 1-342 |
|---|---|---|---|---|---|---|
| $\tau_{\max}$ | 4.90 | 4.0 | 4.0 | 2.83 | 2.83 | 2.32 |
| maxdt | 583.8 | 450 | 300 | 360 | 270 | 225 |
| relerr | 5.97E-7 | 9.45E-7 | 2.39E-4 | 4.44E-7 | 9.71E-4 | 1.04E-6 |

| Method | Strang carryover | ARK324 | ARS343 | ARK2 |
|---|---|---|---|---|
| $\tau_{\max}$ | 1.73 | 1.5 | 1.42 | 1.25 |
| maxdt | 150 | 225 | 240 | 108 |
| relerr | 1.63E-6 | 3.44E-7 | 9.45E-7 | 1.43E-7 |

**6. Conclusion and Acknowledgements.** We derived two new types of IMKG methods for integrating nonhydrostatic atmosphere models with a HEVI partitioning. H-stability regions, while an inexact tool for characterizing stability, were used to derive IMKG methods capable of taking large, stable time-steps and with a relatively short time-to-solution compared to other IMEX methods from the literature. This additional speed comes with the trade-off that IMKG methods are somewhat less accurate than these other methods. For climate and weather prediction this moderate reduction in accuracy is acceptable because it is compensated by significantly shorter run-times. We highlight the IMKG2-244, IMKG2-255, IMKG2-266, and IMKG1-342 methods as having a good balance of speed and accuracy for integrating HEVI models.

We recognize David Gardner, Professor Dan Reynolds, and Carol Woodward for their help in developing and implementing the ARKode-HOMME-NH interface and Professor Paul Ullrich for his expertise and advice. We also thank the reviewers for thoughtful comments and insight.

**7. Appendix.** Double Butcher tableaux for the IMKG methods we derive are given in Equations (7.1)-(7.6). H-stability regions for these methods as well as the non-IMKG methods consider in Section 5 are given in Figures 3-4 with their approximate value of $\tau_{\max}$ in the associated figure caption.

$$
\begin{array}{c|ccccc}
0 & & & & & \\
1/4 & 1/4 & & & & \\
1/3 & & 1/3 & & & \\
1/2 & & & 1/2 & & \\
1 & & & & 1 & \\
\hline
 & & & & 1 &
\end{array}
\qquad
\begin{array}{c|ccccc}
0 & 0 & & & & \\
0 & & 0 & & & \\
2/3 & & & 2/3 & & \\
1/2 & & & 1 & -1/2 & \\
1 & & & & 1 & \\
\hline
 & & & & 1 &
\end{array}
\tag{7.1}
$$

IMKG1-242.

$$
\begin{array}{c|cccccc}
0 & & & & & & \\
1/4 & 1/4 & & & & & \\
1/6 & & 1/6 & & & & \\
3/8 & & & 3/8 & & & \\
1/2 & & & & 1/2 & & \\
1 & & & & & 1 & \\
\hline
 & & & & & 1 &
\end{array}
\qquad
\begin{array}{c|cccccc}
0 & 0 & & & & & \\
0 & & 0 & & & & \\
0 & & & 0 & & & \\
3/4 & & & & 3/4 & & \\
1/2 & & & & 3/2 & -1 & \\
1 & & & & & 1 & \\
\hline
 & & & & & 1 &
\end{array}
\tag{7.2}
$$

IMKG1-252.

$$
\begin{array}{c|cccc}
0 & & & & \\
1/4 & 1/4 & & & \\
2/3 & & 2/3 & & \\
2/3 & 1/3 & & 1/3 & \\
1 & 1/4 & & & 3/4 \\
\hline
 & 1/4 & & & 3/4
\end{array}
\qquad
\begin{array}{c|cccc}
0 & 0 & & & \\
0 & & 0 & & \\
2/3 & & \frac{1-\sqrt{3}}{6} & \frac{3+\sqrt{3}}{6} & \\
2/3 & 1/3 & & -\frac{1+\sqrt{3}}{6} & \frac{3+\sqrt{3}}{6} \\
1 & 1/4 & & & 3/4 \\
\hline
 & 1/4 & & & 3/4
\end{array}
\tag{7.3}
$$

IMKG1-342.

$$
\begin{array}{c|cccc}
0 & & & & \\
1/4 & 1/4 & & & \\
1/3 & & 1/3 & & \\
1/2 & & & 1/2 & \\
1 & & & & 1 \\
\hline
 & & & & 1
\end{array}
\qquad
\begin{array}{c|cccc}
0 & 0 & & & \\
1/4 & & 1/4 & & \\
1/3 & & & 1/3 & \\
1/2 & & & & 1/2 \\
1 & 2/7 & 2/7 & & 3/7 \\
\hline
1 & 2/7 & 2/7 & & 3/7
\end{array}
\tag{7.4}
$$

IMKG2-244.

$$
\begin{array}{c|ccccc}
0 & & & & & \\
1/4 & 1/4 & & & & \\
1/6 & & 1/6 & & & \\
3/8 & & & 3/8 & & \\
1/2 & & & & 1/2 & \\
1 & & & & & 1 \\
\hline
 & & & & & 1
\end{array}
\qquad
\begin{array}{c|cccccc}
0 & 0 & & & & & \\
1/4 & & 1/4 & & & & \\
1/6 & & & 1/6 & & & \\
3/8 & & & & 3/8 & & \\
1/2 & & & & & 1/2 & \\
1 & 2/7 & 2/7 & & & & 3/7 \\
\hline
 & 2/7 & 2/7 & & & & 3/7
\end{array}
\tag{7.5}
$$

IMKG2-255.

$$
\begin{array}{c|cccccc}
0 & & & & & & \\
1/6 & 1/6 & & & & & \\
\frac{2}{15} & & \frac{2}{15} & & & & \\
1/4 & & & 1/4 & & & \\
1/3 & & & & 1/3 & & \\
1/2 & & & & & 1/2 & \\
1 & & & & & & 1 \\
\hline
 & & & & & & 1
\end{array}
\qquad
\begin{array}{c|ccccccc}
0 & 0 & & & & & & \\
1/6 & & 1/6 & & & & & \\
\frac{2}{15} & & & \frac{2}{15} & & & & \\
1/4 & & & & 1/4 & & & \\
1/3 & & & & & 1/3 & & \\
1/2 & & & & & & 1/2 & \\
1 & 3/11 & 3/11 & & & & & 5/11 \\
\hline
 & 3/11 & 3/11 & & & & & 5/11
\end{array}
\tag{7.6}
$$

IMKG2-266.

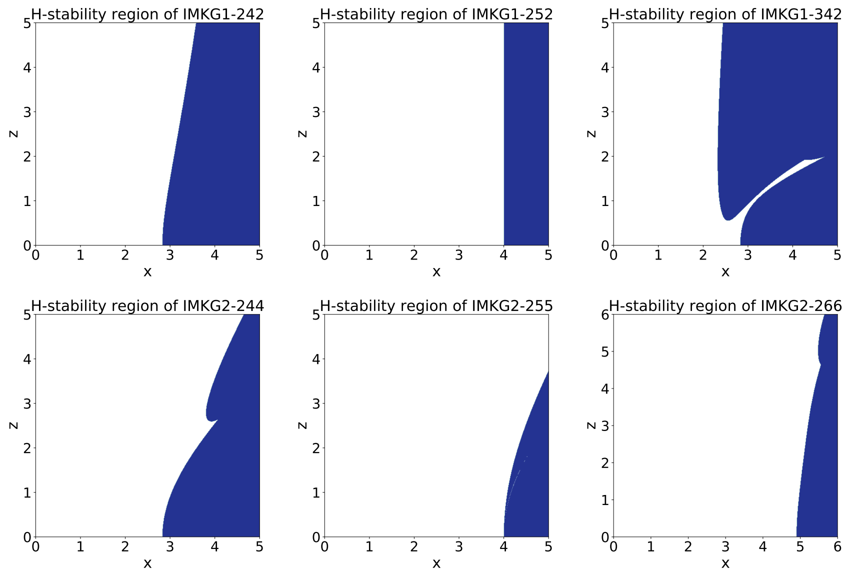


Fig. 3: H-stability regions of the IMKG1 and IMKG2 methods: IMKG1-242 (top left, $\tau_{\max} = 2\sqrt{2}$), IMKG1-252 (top center, $\tau_{\max} = 4$), IMKG1-342 (top right, $\tau_{\max} \approx 2.32$), IMKG2-244 (bottom left, $\tau_{\max} = 2\sqrt{2}$), IMKG2-255 (bottom center, $\tau_{\max} = 4$), IMKG2-266 (bottom right, $\tau_{\max} = 2\sqrt{6}$). The unshaded region denotes values $(x, z)$ contained in the H-stability region (eigenvalues of $R_H(x, z)$ less than 1 in modulus) while the blue shaded region denotes values $(x, z)$ outside the H-stability region (eigenvalues of $R_H(x, z)$ are at least 1 in modulus).

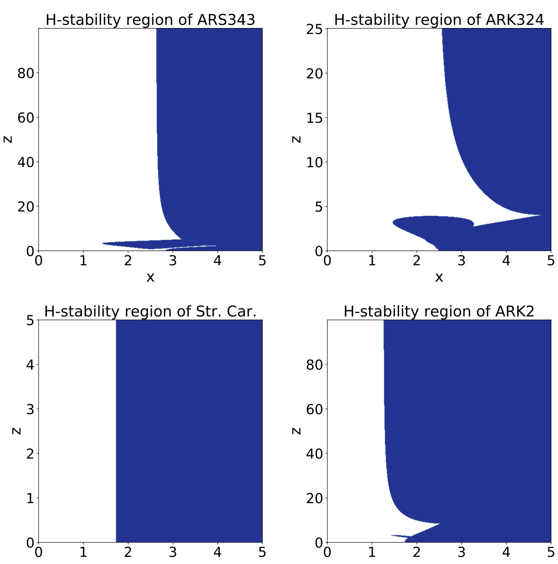


Fig. 4: H-stability regions of non-IMKG methods: ARS343 (top left, $\tau_{\max} \approx 1.42$), ARK324 (top right, $\tau_{\max} \approx 1.5$), Strang carryover (bottom left, $\tau_{\max} \approx 1.73$), and ARK2 (bottom right, $\tau_{\max} \approx 1.25$). The unshaded region denotes values $(x, z)$ contained in the H-stability region (eigenvalues of $R_H(x, z)$ less than 1 in modulus) while the blue shaded region denotes values $(x, z)$ outside the H-stability region (eigenvalues of $R_H(x, z)$ are at least 1 in modulus).

## REFERENCES


[1] Abdi, D., Giraldo, F., Constantinescu, M., Carr III, L., Wilcox, L., and Warburton, T., *Acceleration of the IMplicit-EXplicit non-hydrostatic unified model of the atmosphere (NUMA) on manycore processors*, Int. J. High Perform C., 33 (2019), https://doi.org/10.1177/1094342017732395.

[2] Ascher, U., Ruuth, S., and Spiteri, R., *Implicit-explicit Runge-Kutta methods for time-dependent partial differential equations*, Appl. Numer. Math., 25 (1997), pp. 151–167, https://doi.org/10.1137/0732037.

[3] T. Davies, A. Staniforth, N. Wood, and J. Thuburn, *Validity of anelastic and other equation sets as inferred from normal-mode analysis*, Quarterly Journal of the Royal Meteorological Society, 129 (2003), pp. 2761 – 2775, https://doi.org/10.1256/qj.02.1951.

[4] Dennis, J., Edwards, J., Evans, K., Guba, O., Lauritzen, P., Mirin, A., St-Cyr, A., Taylor, M., and Worley, P., *CAM-SE: A scalable spectral element dynamical core for the Community Atmosphere Model*, Int. J. High Perform C., 26 (2012), pp. 74–89, https://doi.org/10.1177/1094342011428142.

[5] Durran, D. and Blossey, P., *Implicit-explicit multistep methods for fast-wave-slow-wave problems*, Mon. Weather Rev., 140 (2012), pp. 1307–1325, https://doi.org/10.1175/MWR-D-11-00088.1.

[6] K. J. Evans, R. K. Archibald, D. J. Gardner, M. R. Norman, M. A. Taylor, C. S. Woodward, and P. H. Worley, *Performance analysis of fully explicit and fully implicit solvers within a spectral element shallow-water atmosphere model*, The International Journal of High Performance Computing Applications, 33 (2019), pp. 268–284, https://doi.org/10.1177/1094342017736373.

[7] Evans, K., Lauritzen, P., Mishra, S., Neale, R., Taylor, M., and Tribbia, J., *AMIP simulation with the CAM4 spectral element dynamical core*, J. Climate, 26 (2013), pp. 689–709, https://doi.org/10.1175/JCLI-D-11-00448.1.

[8] Frank, J., Hundsdorfer, W., and Verwer, J., *On the stability of implicit-explicit linear multistep methods*, Appl. Numer. Math., 25 (1997), pp. 193–205, https://doi.org/10.1016/S0168-9274(97)00059-7.

[9] Gardner, D., Guerra, J., Hamon, F., Reynolds, D., Ullrich, P., and Woodward, C., *Implicit-explicit (IMEX) Runge-Kutta methods for non-hydrostatic atmospheric models*, Geosci. Model Dev., 11 (2018), pp. 1497–1515, https://doi.org/10.5194/gmd-2017-285.

[10] Gardner, D., Reynolds, D., Hamon, F., Woodward, C., Ullrich, P., Guerra, J., Lelbach, B., and Banide, A., *Tempest+ARKode IMEX tests*, Geosci. Model Dev., 11 (2018), pp. 1497–1515, https://doi.org/10.5194/gmd-11-1497-2018.

[11] Ghosh, D. and Constantinescu, E., *Semi-implicit time integration of atmospheric flows with characteristic-based flux partitioning*, SIAM J. Sci. Comput., 38 (2016), pp. A1848–A1875, https://doi.org/10.1137/15M1044369.

[12] Giraldo, F., Kelly, J., and Constantinescu, E., *Implicit-explicit formulations of a three-dimensional nonhydrostatic unified model of the atmosphere (NUMA)*, SIAM J. Sci. Comput., 35 (2013), pp. B1162–B1194, https://doi.org/10.1137/120876034.

[13] Giraldo, F., Rastelli, M., and Läuter, M., *Semi-implicit formulations of the Navier-Stokes equations: Application to nonhydrostatic atmospheric modeling*, SIAM J. Sci. Comput., 32 (2010), pp. 3394–3425, https://doi.org/10.1137/090775889.

[14] Guerra, J. and Ullrich, P., *A high-order staggered finite-element vertical discretization for non-hydrostatic atmospheric models*, Geosci. Model Dev., 9 (2016), pp. 2007–2029, https://doi.org/10.5194/gmd-9-2007-2016.

[15] Hairer, E., *Order conditions for numerical methods for partitioned ordinary differential equations*, Numer. Math., 36 (1981), pp. 431–445, https://doi.org/10.1007/BF01395956.

[16] Hairer, E., Bader, G., and Lubich C., *On the stability of semi-implicit methods for ordinary differential equations*, BIT, 22 (1982), pp. 211–232, https://doi.org/10.1007/BF01944478.

[17] Hairer, E. and Wanner, G., *Solving Ordinary Differential Equations II. Stiff and Differential-Algebraic Problems*, Springer-Verlag Berlin Heidelberg, Second ed., 1996, https://doi.org/10.1007/978-3-642-05221-7.

[18] Hindmarsh, A., Brown, P., Grant, K., Lee, S., Serban, R., Shumaker, D., and Woodward, C., *SUNDIALS: Suite of nonlinear and differential/algebraic equation solvers*, ACM T. Math. Software, 31 (2005), pp. 363–396, https://doi.org/10.1145/1089014.1089020.

[19] Jeltsch, R. and Nevanlinna, O., *Stability of explicit time discretizations for solving initial value problems*, Numer. Math., 37 (1981), pp. 61–91, https://doi.org/10.1007/BF01396187.

[20] Kasahara, A., *Various vertical coordinate systems used for numerical weather prediction*, Mon. Weather Rev., 102 (1974), pp. 509–522, https://doi.org/10.1175/1520-0493(1974)

102⟨0509:VVCSUF⟩2.0.CO;2.

[21] Kennedy, C. and Carpenter, M., *Additive Runge-Kutta schemes for convection-diffusion-reaction equations*, NASA Technical Memorandum, NASA/TM-2001-211038, Langley Research Center, Hampton, VA, 2001.

[22] Kennedy, C. and Carpenter, M., *Additive Runge-Kutta schemes for convection-diffusion-reaction equations*, Appl. Numer. Math., 44 (2003), pp. 139–181, https://doi.org/10.1016/S0168-9274(02)00138-1.

[23] Kinnmark, I. and Gray, W., *One step integration methods with maximum stability regions*, Math. Comput. Simulat., XXVI (1984), pp. 84–92, https://doi.org/10.1016/0378-4754(84)90039-9.

[24] Kinnmark, I. and Gray, W., *One step integration methods with third-fourth order accuracy with large hyperbolic stability limits*, Math. Comput. Simulat., XXVI (1984), pp. 181–188, https://doi.org/10.1016/0378-4754(84)90056-9.

[25] Laprise, R., *The Euler equations of motion with hydrostatic pressure as an independent variable*, Mon. Weather Rev., 102 (1992), pp. 197–207, https://doi.org/10.1175/1520-0493(1992)120⟨0197:TEEOMW⟩2.0.CO;2.

[26] Lock, S.-J., Wood, N., and Weller, H., *Numerical analyses of Runge-Kutta implicit-explicit schemes for horizontally explicit, vertically implicit solutions of atmospheric models*, Q. J. Roy. Meteor. Soc., 140 (2014), pp. 1654–1669, https://doi.org/10.1002/qj.2246.

[27] Lorenz, E., *Energy and numerical weather prediction*, Tellus, 12 (1960), pp. 364–373, https://doi.org/10.1111/j.2153-3490.1960.tb01323.x.

[28] Satoh, M., *Conservative scheme for the compressible nonhydrostatic models with the horizontally explicit and vertically implicit time integration scheme*, Mon. Weather Rev., 130 (2002), pp. 1227–1245, https://doi.org/10.1175/1520-0493(2002)130⟨1227:csftcn⟩2.0.co;2.

[29] Simmons, A.J. and Burridge, D.M., *An energy and angular-momentum conserving vertical finite-difference scheme and hybrid vertical coordinates*, Mon. Weather Rev., 109 (1981), pp. 758–766, https://doi.org/10.1175/1520-0493(1981)109⟨0758:AEAAMC⟩2.0.CO;2.

[30] Tapp, M. and White, P., *A non-hydrostatic mesoscale model*, Q. J. Roy. Meteor. Soc., 102 (1976), pp. 277–296, https://doi.org/10.1002/qj.49710243202.

[31] Taylor, M., Guba, O., Steyer, A., Ullrich, P., Hall, D., and Eldred, C., *An energy consistent discretization of the nonhydrostatic equations in primitive variables*, J. Adv. Model. Earth Syst., 12 (2020), https://doi.org/10.1029/2019MS001783.

[32] Taylor, M., Tribbia, J., and Iskandarani, M., *The spectral element method for the shallow water equations on the sphere*, J. Comput. Phys., 130 (1997), pp. 92–108, https://doi.org/https://doi.org/10.1006/jcph.1996.5554.

[33] Taylor, M.A. and Fournier, A., *A compatible and conservative spectral element method on unstructured grids*, J. Comput. Phys., 229 (2010), pp. 5879–5895, https://doi.org/10.1016/j.jcp.2010.04.008.

[34] Ullrich, P. and Jablonowski, C., *Operator-split Runge-Kutta-Rosenbrock methods for nonhydrostatic atmospheric models*, Mon. Weather Rev., 140 (2012), pp. 1257–1284, https://doi.org/10.1175/MWR-D-10-05073.1.

[35] Ullrich, P., Jablonowski, C., Kent, J., Lauritzen, P., Nair, R., and Taylor, M., *Dynamical core model intercomparison project (DCMIP) 2012 Test Case Document v.1.7*, Tech. Rep., (2012).

[36] G. K. Vallis, *Atmospheric and Oceanic Fluid Dynamics: Fundamentals and Large-Scale Circulation*, Cambridge University Press, 2017, https://doi.org/10.1017/9781107588417.

[37] van der Houwen, P., *Explicit Runge-Kutta formulas with increased stability boundaries*, Numer. Math., 20 (1972), pp. 149–164, https://doi.org/10.1007/BF01404404.

[38] van der Houwen, P., *Construction of integration formulas for initial-value problems*, North-Holland, Amsterdam, 1977.

[39] van der Houwen, P., *The development of Runge-Kutta methods for partial differential equations*, Appl. Numer. Math., 20 (1996), pp. 261–272, https://doi.org/10.1016/0168-9274(95)00109-3.

[40] Vichnevetsky, R., *New stability theorems concerning one-step methods for ordinary differential equations*, Math. Comput. Simulat., XXV (1983), pp. 199–205, https://doi.org/10.1016/0378-4754(83)90092-7.

[41] Vogl, C., Steyer, A., Reynolds, D., Ullrich, P., and Woodward, C., *Evaluation of implicit-explicit Runge-Kutta integrators for the HOMME-NH dynamical core*, J. Adv. Model. Earth Syst., (2019), https://doi.org/10.1029/2019MS001700.

[42] Weller, H., Lock, S.-J., and Wood, N., *Runge-Kutta IMEX schemes for the horizontally explicit/vertically implicit (HEVI) solution of wave equations*, J. Comput. Phys., 252 (2013), pp. 365–381, https://doi.org/10.1016/j.jcp.2013.06.02.